Pattern-based Reconstruction of K-level Images from Cutsets

Shengxin Zha, *Member, IEEE,* Daizong Tian,Thrasyvoulos N. Pappas, *Fellow, IEEE,*

***Abstract*—We present a pattern-based approach for reconstructing a K-level image from cutsets, dense samples taken along a family of lines or curves in two- or three-dimensional space, which break the image into blocks, each of which is typically reconstructed independently of the others. The pattern-based approach utilizes statistics of human segmentations to generate a codebook of patterns, each of which represents a pair of a block boundary specification and the corresponding pattern in the block interior. We develop the approach for rectangular cutset topologies and show that it can be extended to general periodic sampling topologies. We also show that, for bilevel cutset reconstruction, the pattern-based can be combined with the previously proposed cutset-MRF approach to substantially reduce the size of the codebook with a slight increase in reconstruction error. In addition, we present an algorithm for segmenting the cutset samples of an original grayscale or color image, followed by reconstruction of the full segmentation field via the pattern-based approach. Experimental results show that the proposed approaches outperform the cutset-MRF approaches in terms of both reconstruction error rate and perceptual quality. Moreover, this is accomplished without any side information about the structure of the block interior. Systematic comparisons of the performance of different sampling topologies are also provided.**

***Index Terms*—Image sampling, segmentation, reconstruction, interpolation**

I. Introduction

Cutset sampling is a recently proposed approach for gathering data along a family of lines or curves in two- or three-dimensional space. For example, Figure 1 shows cutset sampling along rows and columns of a dense two-dimensional Cartesian grid, and compares it to uniform sampling. The advantages of cutset sampling were first exploited for lossy bilevel image compression [1]–[3]. Apart from compression efficiency, cutset sampling may be dictated by physical constraints, e.g., deploying sensors along city streets or forest service roads, or when sampling from moving vehicles (trucks, buses, ships, airplanes) for which a cutset topology substantially reduces the number of passes to be made by the vehicle over the area of interest. Cutset sampling may also be beneficial for wired sensor networks, for which the cutset topology substantially reduces the number and length of wires, or for wireless sensor networks, for which the cutset topology facilitates energy efficient communication among sensors [4].

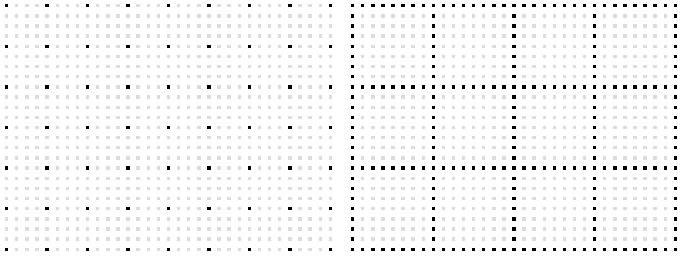

Fig. 1: Uniform versus cutset sampling on a Cartesian grid

In cutset sampling, the samples are typically one or more scalar values collected at the location of each sensor, which can represent physical measurements (temperature, salinity, pollution), image intensities (grayscale, color, multispectral), or region labels in a segmentation map. Given the samples on the cutset, the task is then to recover (interpolate) the samples in the rest of the field, based on an underlying model, typically uniform regions separated by sharp transitions at smooth or piecewise smooth boundaries.

In this paper, we will focus on the cutset topology shown in Figure 1, whereby the samples are taken every N rows and every N columns, resulting in $(N+1)\times(N+1)$ square blocks, each of which shares $4N$ cutset samples on the block boundaries with the neighboring blocks and encloses $(N-1)\times(N-1)$ unsampled Cartesian nodes ($N = 8$ in the figure). Note that the average sampling densities of the uniform and cutset topologies are not the same; what really matters is the sample availability or the efficiency with which the samples can be collected, encoded, or transmitted. We will assume that the cutset samples represent region labels, taking values in the set $\{1, 2, \ldots, K\}$, and that the numbers have no other significance. As we will see, the assumption is that the images or data fields we are sampling have been segmented, either before or after sampling.

The primary goal of this paper is the reconstruction of the missing Cartesian samples from the cutset. We will assume that the underlying K-level images ($K \geq 2$) belong to a broad class of images, in which the regions are separated by smooth, or piecewise smooth boundaries. We will refer to this as the *smoothness criterion* [3]. Such images may arise in graphics, line drawings, pen and ink sketches, or logos, but our primary interest is on segmentation maps, from which decisional, regional, or semantic information can be extracted. Given that the underlying image satisfies the smoothness criterion, the aim of the K-level cutset reconstruction is to extend segments from the cutset to the full field with piecewise smooth contours. Figure 2 illustrates an example of K-level cutset sampling and reconstruction. In

Manuscript received 16 March 2021; revised 5 November 2021, 8 April 2022, and 29 May 2022; accepted 5 June 2022. Date of publication 11 August 2022; date of current version 26 August 2022. This work was supported in part by the Office of Naval Research (ONR) under Grant N00014-17-1-2707. Parts of this work were presented at the 2015 ICIP Proceedings [DOI: 10.1109/ICIP.2015.7351423] and the 2016 ICASSP Proceedings [DOI: 10.1109/ICASSP.2016.7471963]. The associate editor coordinating the review of this manuscript and approving it for publication was Prof. Riccardo Leonardi. (Corresponding author: Thrasyvoulos N. Pappas.)

Shengxin Zha is with Facebook Inc., Menlo Park, CA 94025 USA.

Daizong Tian and Thrasyvoulos N. Pappas are with the Department of Electrical and Computer Engineering, Robert R. McCormick School of Engineer-ing and Applied Science, Northwestern University, Evanston, IL 60208 USA (e-mail: pappas@ece.northwestern.edu).

This article has supplementary downloadable material available at https://doi.org/10.1109/TIP.2022.3196171, provided by the authors.

Digital Object Identifier 10.1109/TIP.2022.3196171

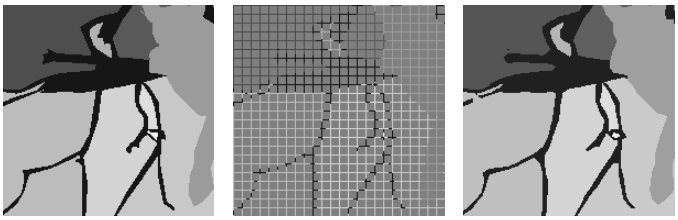

Original Cutset samples Reconstruction

Fig. 2: Cutset sampling and reconstruction

addition to cutset sampling and reconstruction of a K-level image, we will consider cutset sampling of a grayscale or color image, segmentation of the cutset, and reconstruction of the full segmentation field.

The 2-level reconstruction was considered in the context of lossy bilevel image compression [1]–[3]. The key idea of the lossy cutset coding (LCC) approach by Reyes *et al.* is to encode and transmit the pixels on a cutset, and to reconstruct the interiors of the blocks formed by the grid using a Markov random field (MRF) model. The role of the MRF model is to enforce the reconstruction of the smoothest image that is consistent with the samples on the cutset. The term *cutset* was adopted because, when second-order MRF models are used, the reconstructions of the block interiors are decoupled [1], [2]. The role of a cutset is to preserve key structural information of the image, from which the full image field can be reconstructed. Reyes *et al.* [1], [2] found explicit rules for optimal reconstructions for boundary specifications that contain up to two runs of black (and two runs of white) pixels. Zha *et al.* [3] proposed a hierarchical version of LCC that adapts the grid size to local image detail. We will refer to the MRF-based reconstruction as the *cutset-MRF* approach.

The bilevel cutset reconstruction has also been used as an intermediate step (providing segment information) for grayscale cutset reconstruction based on a Gaussian-MRF model [5]. A variation of this approach, based on three-level plane fitting and the Gaussian-MRF model, was introduced in [6]. Prelee *et al.* [6] also considered the K-level reconstruction for $K > 2$, and suggested heuristic rules that favor fewer long smooth boundaries between regions; however, the problem remains quite open. An alternative approach obtains grayscale reconstructions directly based on orthogonal gradients on cutsets [7].

Reyes *et al.* [1], [2] found that the optimal reconstruction does not always provide an accurate representation of the original bilevel image, and used side information in the form of a *connection bit* to signify which segments of black or white pixels (runs) on the block boundary should be connected in the reconstruction. They found that reconstructions based on the connection bit are significantly better at preserving the structural information of the image. Zha *et al.* [3] introduced additional connection bits, which provide valuable structural information for larger grid sizes ($N > 8$). However, in most real-world scenarios, apart from compression applications, such side information is not available. Thus, the first challenge is to recover as much structural information as possible without the use of connection bits. Moreover, the explicit rules for optimal reconstruction that Reyes *et al.* [1], [2] found do not apply to images with $K > 2$ levels, and one has to resort to iterative reconstruction, which is extremely time-consuming. Thus, the second challenge is to find efficient and accurate algorithms for reconstruction of piecewise smooth K-level images from cutsets for the $K > 2$ case.

In this paper we explore an alternative, *pattern-based* approach for K-level cutset reconstruction that relies on statistics of human segmentations of natural images to generate a codebook of patterns that correspond to a set of boundary specifications. The idea is to find the pattern that is most likely to have resulted in a given boundary specification. Thus, the structural decisions (whether two runs should be connected) are made based on statistics (how often they are connected in segmentations of natural images). We show that the performance of the pattern-based approach results in lower reconstruction error rate and better visual appearance than the cutset-MRF approaches. The pattern-based approach also applies to a broader class of images, including K-level images ($K \geq 2$), and general sampling topologies, such as non-intersecting lines, hexagonal cutsets, and uniform point samples.

In addition, we show that the pattern-based and MRF-based approaches can be combined for bilevel cutset reconstruction. The idea is to utilize statistics of human segmentations to determine structural information and then to reconstruct piecewise smooth segment contours based on an MRF model. Such a combination slightly increases the reconstruction error rate compared to the pure pattern-based approach, but substantially reduces the codebook size, thus reducing both the storage overhead and the testing time. We show that the combined approach, which we call *PAT/MRF* approach, still outperforms the cutset-MRF approaches when there are no connection bits. However, as we discussed above, there is no efficient MRF-based reconstruction for $K > 2$, so the PAT/MRF approach only applies to bilevel reconstruction.

The main contributions of this paper are summarized as follows

- We present a pattern-based K-level cutset reconstruction approach that utilizes statistics from human segmentations of natural images to generate a codebook of patterns, without additional information (connection bits).
- We extend the pattern-based approach to general periodic sampling topologies.
- We combine the pattern-based and cutset-MRF approaches into the PAT/MRF approach for bilevel cutset reconstruction.
- In addition, we show how the adaptive clustering algorithm [8] can be modified to segment the cutset samples of the original grayscale or color image, followed by reconstruction of the full segmentation field via the pattern-based approach.

The key ideas on pattern-based cutset reconstruction were introduced in two conference papers [9], [10]. This paper provides a comprehensive presentation of the approaches with additional details, analysis, and extended experimental results.

The remainder of this paper is organized as follows. Section II reviews the related work. Section III introduces the pattern-based approach. Section VI demonstrates the experimental results. Section VII concludes this paper.

II. Related Work

Cutsets have been studied in bilevel image compression [1], [2], [11], image sampling and reconstruction [5]–[7], [12], [13], and sensor networks [4], [14]. In this section we review bilevel cutset reconstruction based on MRF and the most relevant work on K-level and bilevel cutset reconstructions.

A. MRF-Based Bilevel Cutset Reconstruction

A bilevel image can be modeled by a Markov random field (MRF). A second-order MRF is defined on an 8-connected graph,

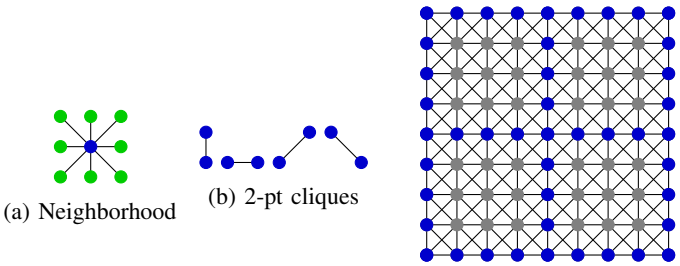

(a) Neighborhood (b) 2-pt cliques (c) Cutset (blue); unsampled interior nodes (gray)

Fig. 3: MRF and cutset associated with 2-point cliques

in which each node (pixel or point) belongs to a second-order neighborhood shown in Figure 3a. Of all the cliques (groups of points that are neighbors of each other) that are associated with such a neighborhood, we use only four types of two-point cliques: horizontal, vertical, diagonal, and anti-diagonal, as shown in Figure 3b. Let x_s denote the value of a node s. The image values $\mathbf{x}$ are modeled by the probability density function

$$p(\mathbf{x}) = \frac{1}{Z}\exp\{-\sum_{C} V_C(\mathbf{x})\}, \quad \mathbf{x} \in \{0,1\} \tag{1}$$

$$V_C(\mathbf{x}) = \begin{cases} -\beta, & x_s = x_q, (s,q) \in C \\ +\beta, & x_s \neq x_q, (s,q) \in C \end{cases} \tag{2}$$

where Z is a normalization constant, β is a positive constant, C denotes a specific clique, and s and q denote the nodes in the clique C. Maximizing $p(\mathbf{x})$ is equivalent to minimizing the number of odd bonds (black and white transitions along the segment contours). This model has been the basis for cutset-based bilevel image reconstruction and compression [1], [2].

A cutset subdivides an image into blocks, each of which includes the cutset nodes on the block boundary shared by adjacent blocks and the unsampled nodes in block interior, as illustrated in Figure 3c. With the second-order MRF model, the cutset decouples the blocks, in the sense that the reconstruction of each block interior is independent of the reconstruction of the other blocks. The reconstruction in [1], [7] is based on a maximum a posteriori (MAP) estimate of the interior pixels of a block, given the values of the boundary pixels, which reduces to finding the bilevel block interior that in combination with the boundary has the fewest black-white transitions between pixels. In the following, we will refer to the cutset-MRF approach with a second-order MRF model as MRF_2. Note that a digitized straight line representation of segment contours is among the optimal reconstructions [3]. Accordingly, in the experimental results of Section VI, we will use straight lines for MRF_2 reconstructions.

There are two main limitations of the cutset-MRF approach. First, an efficient reconstruction algorithm is currently only available for bilevel images sampled on rectangular cutsets. Extension to multiple levels and other sampling topologies may be possible but is not obvious. Second, the quality of reconstruction based on second-order MRF model depends highly on the connection bits, which are not available without access to the full bilevel image.

A two stage cutset-MRF approach that relies on a hybrid MRF model to reconstruct bilevel images from cutsets was proposed in [13]; we will refer to this as the *hybrid-MRF* approach or MRF_h. MRF_h separates the structural decisions that indicate the connectivities of pixels in black and white regions from the contour reconstruction details. The structural decisions rely on a hybrid MRF model, in which the nodes are associated with 3-point cliques or 2-point cliques that align in vertical, horizontal, and diagonal lines. The contour details are generated by the second-order MRF model given the connectivities of nodes on the boundary. The MRF_h approach provides better reconstruction than MRF_2 when connection bits are not available. However, as we will show in Section VI, MRF_h cannot match the performance of the proposed pattern-based approach or that of the more efficient combined pattern-based/cutset-MRF approach. As we will see, the advantages of the proposed approaches become more obvious as the image structure becomes more complicated.

B. Interpolation, Inpainting, Restoration, and Neural Nets

Cutset reconstruction can be viewed as a form of image interpolation, where the samples are densely located on intersecting lines with relatively large gaps in between. The classic image interpolation algorithms, such as bilinear, bicubic, and polynomial interpolation, do not work for cutset reconstruction. In Section VI, we will show that a variation of bilinear interpolation, adapted for region labels, and simple nearest neighbor interpolation result in clearly inferior performance.

Image inpainting is closely related to cutset reconstruction in that it attempts to continue the isophote lines (equal level lines) smoothly from the boundary into the reconstructed regions. The well-known inpainting approach by Bertalmio *et al.* [15] is based on the Navier-Stokes equations for fluid dynamics, which project the gradient of the smoothness of the image intensity in the direction of the isophotes and formulate the problem as a discrete approximation of a partial differential equation (PDE). A specialized PDE-based approach for bilevel image inpainting was achieved with a modified Cahn-Hilliard equation [16]. Another inpainting approach, first proposed in [17], propagates the weighted average of boundary pixel values along with their gradients into the missing region and uses a fast marching method, which is relatively faster than previous PDE-based approaches. However, since these approaches rely on gradients in the boundary neighborhood, they are not suited for cutset reconstruction, where only a one-pixel-wide boundary is available. An exemplar-based image inpainting approach was proposed in [18], and aims to remove large objects by simultaneous propagation of texture and structure information. However, it is designed for filling a target region from relatively large known regions, which are not available in a cutset. Huang *et. al.* proposed a method for automatically guiding patch-based image completion using mid-level structural cues [19]. This method produces strong image inpainting results. However, the mid-level structural cues are based on image features that can not be extracted from the cutsets.

Cutset reconstruction is related to, but differs from typical image restoration problems, such as image denoising and image deblurring, where the former consider reconstructing the full field from samples while the latter consider recovering or enhancing an image from noise, blurriness, or damage.

Eslami *et al.* [20] used a deep Boltzmann machine ("shape Boltzmann machine") to model object shape for image segmentation and object detection. However, the approach they proposed does not work for the cutset reconstruction problem because the network input consists of pixels of an entire image block rather than its boundaries. The authors discuss shape completion from missing image sections but, in the results they show, the missing blocks are surrounded by solid areas of pixels, not lines. When we

tried to use their algorithm for cutset reconstruction, the results were very poor. In addition, their algorithm has only been shown to reconstruct a limited number of object categories, in contrast to the pattern-based reconstruction that can handle arbitrary shapes that meet the smoothness criterion.

In summary, one of the main challenges for cutset reconstruction is that it is based on one-pixel-wide lines of samples with relatively large gaps between the lines, as compared to higher sampling densities considered in other image interpolation problems, and thicker boundaries or larger neighborhoods in typical image inpainting problems.

III. Pattern-based Approach for K-level Cutset Reconstruction

In this section we introduce the pattern-based approach for K-level cutset reconstruction that relies on statistics of human segmentations of natural images. We first develop the approach for rectangular cutset topologies, and then extend it to general periodic sampling topologies.

In the following, we first present a probabilistic formulation of the problem. We then describe the construction of a database (DB) of K-level cutset block patterns that will enable the association of a boundary specification with the most probable interior pattern. Finally, we propose a rule for matching the boundary specification of a given block with a boundary pattern in the database and the associated interior pattern.

A. Probabilistic Problem Formulation

Let $\mathbf{S}$ be the set of all $(N+1)\times(N+1)$ blocks of region labels, sampled on a Cartesian grid, and taking values in the set $\{1,2,\ldots,K\}$. Each element $(\mathbf{b}^j,\mathbf{x}^j)$ of $\mathbf{S}$ consists of a boundary specification $\mathbf{b}^j$ and an interior pattern $\mathbf{x}^j$, where j is the element index. Each boundary specification will be represented as an n-dimensional vector $\mathbf{b}^j=[b_0^j,b_1^j,\ldots,b_n^j]^T$ that includes the $n=4N$ cutset samples, and the block interior will be represented as an m-dimensional vector $\mathbf{x}^j=[x_0^j,x_1^j,\ldots,x_m^j]^T$ that includes the $m=(N-1)\times(N-1)$ interior samples.

If we assume a probabilistic model for $\mathbf{S}$, the Bayesian estimator of the interior $\mathbf{x}$ given the boundary $\mathbf{b}$ is given by $\hat{\mathbf{x}}(\mathbf{b})=E\{\mathbf{x}|\mathbf{b}\}$, which minimizes the expected mean square error $E\{(\hat{\mathbf{x}}(\mathbf{b})-\mathbf{x})^2\}$. In practice, the expected value is estimated by an empirical average. If $\mathbf{S}_o\subset\mathbf{S}$ is the set of observed blocks in the database of natural image segmentations, then

$$\hat{x}_i^{\mathrm{B}}(\mathbf{b})=E\{x_i|\mathbf{b}\}\approx\sum_{j\in\mathbf{S}_o}x_i^j f(x_i^j|\mathbf{b}^j=\mathbf{b})\;\; i=0,\ldots,m \quad (3)$$

where f denotes the frequency that an interior pattern $\mathbf{x}^j$ corresponds to a boundary pattern $\mathbf{b}^j$. However, since in K-level images the pixel values represent levels rather than grayscale values, it does not make sense to compute a weighted sum of pixel labels, and thus, we cannot use the Bayesian estimator of (3). Instead, we use the maximum likelihood (ML) estimator, that is, the most frequent level at each pixel.

$$\hat{x}_i^{\mathrm{ML}}(\mathbf{b})=x_i^J,\;\; J=\underset{j\in\mathbf{S}_o}{\arg\max}\, f(x_i^j|\mathbf{b}^j=\mathbf{b})\;\; i=0,\ldots,m \quad (4)$$

When $\mathbf{S}_o$ is large and representative of natural image segmentations, the ML estimate provides the most likely reconstruction to appear in a natural image.

Fig. 4: K-level human segmentations of natural images

The next step will be to collect a database of K-level cutset block patterns and to organize the boundary specifications in the database into equivalence classes by applying a set of normalization rules. This will enable the association of each boundary specification in the database with the most probable interior pattern, based on (4).

B. Construction of K-level Pattern Database

A K-level cutset block pattern database is built from human segmentations of natural images; examples of such K-level images are shown in Figure 4. These K-level images are then decoupled into blocks, each processed independently from other blocks. We make the following assumptions: (i) the region boundaries of the K-level field are piecewise smooth; and (ii) there are no islands in the block interior, i.e., all components in the block interior are connected to the block boundaries. Assumption (i) is a direct extension of the piecewise smooth region boundary assumption of bilevel images [3]. Assumption (ii) states that the sampling step of a cutset should be fine enough to capture information about all segments.

An explicit listing of all the distinct instances of boundary specifications for K-level images results in polynomial complexity, $O(K^{4N})$, where N denotes the cutset sampling step. As we saw, a cutset block consists of $4N$ boundary pixels (shared with adjacent blocks), and $(N-1)^2$ interior pixels. However, since the pixel values are just labels and have no other significance (and hence the values for each class can be arbitrarily reassigned), and the actual number of runs of pixels of the same label that can occur on the boundary of an $N\times N$ block is small (typically 1-6), the overall number of boundary patterns is reasonably small to be examined but large enough to be non-trivial.

In order to reduce the number of distinct boundary patterns and to increase the amount of data collected for each boundary pattern, we use the following ***normalization rules:***

1) Rotate each block by 0°, 90°, 180°, or 270°so that the first pixel (assuming clockwise scanning) of the longest run is at the top of the boundary, excluding the top-right corner.
2) Index the level of the longest run with 0.
3) Index the levels of the remaining runs incrementally according to their discovery order in a clockwise scan of the block boundary, starting from the longest run.
4) Note that for each boundary index there is a corresponding original boundary level, which is consistent with the block interior labels.

By doing so, the number of possible distinct boundary specifications for a given number of runs, R, is upper bounded by $4^{R-1}N^R(k-1)^{R-2}$, as compared to $4^RN^RK(K-1)^{R-1}$ without normalization, where k and K denote the number of distinct levels in a block and an image, respectively, and $k\le K$. For example, for $N=8$, $k=K=4$, and $R=6$, we have $2^{34}=17*10^9$ specifications with normalization and $2^{40}=10^{12}$ without. These numbers are still too big. However, when we take into account

Fig. 5: Sampling topologies with periodic structures

the fact that one-pixel runs are extremely rare and isolated and typical runs are several pixels long, the numbers are considerably smaller. Specific numbers can be found in Section VI.

In constructing the database, we collect all the interior patterns that correspond to a given boundary specification, and then use (4) to find the most likely interior pattern to associate with that boundary specification. If there are not enough instances of a boundary specification (e.g., less than 5), then it is merged with a similar boundary specification that differs by at most one pixel. In such cases, there are separate entries in the database that associate these boundary specifications with the same interior pattern.

The next step will be to propose a rule for matching the boundary specification of a given block with a boundary pattern in the database.

C. Pattern Retrieval

We now consider the reconstruction of the full K-level image from a cutset. We partition the cutset into $N \times N$ blocks; each block has N-point overlap with its 4-connected neighbors and 1-point overlap with its 8-connected neighbors. A query block boundary is normalized using the same rules that were used for the database construction. If there is an exact match for a query block boundary in the database, then we use the interior pattern associated with the specification as the reconstruction of the block interior. If an exact match cannot be found, the reconstruction is based on the closest match by allowing a shift by one pixel in two consecutive runs (shortening one run and lengthening the other by one pixel). If no such match is found, then we iteratively merge the shortest run into its neighbors (by flipping the color of the shortest run to the color of its longest neighboring run) until a match is found. If several matches are equally close, then the most frequent of the block interior patterns associated with these matches is used. This process is summarized in Algorithm 1. The reconstruction then proceeds with inverting the normalization operations that were used to match the original query.

D. Generalized Cutset Sampling and Reconstruction

The pattern-based cutset reconstruction approach we presented in the previous section assumes square cutsets, i.e., cutsets sampled on evenly spaced rows and columns of Cartesian grids. The pattern-based approach can be extended to generalized sampling topologies that consist of periodic structures, such as the evenly spaced straight lines, zig-zagged lines, and hexagonal blocks, shown in Figure 5 along with the corresponding period of the structure. The pattern-based approach can also be used for more conventional sampling topologies, such as uniform sampling, periodic random sampling (a random block is periodically repeated), and periodic blue noise, as well as combinations of cutset and conventional sampling topologies [10].

Algorithm 1: Boundary Pattern Matching

Input : Q: Query boundary vector
r: Number of runs in Q
$l_1, \ldots, l_r$: Run lengths in Q
B_m, $m = 1, \ldots, M$: Boundary vectors in DB
r_m: Number of runs in B_m
$l_1, \ldots, l_{r_m}$: Run lengths in B_m
Output: q: Index of closest matching boundary vector B_q
Preprocessing Step:
Apply normalization rules to Q and B_m, $m = 1, \ldots, M$
while $r > 0$ **do**
  $s = 0$
  for $m = 1, \ldots, M$ **do**
    if $r_m \neq r$ **then**
      continue
    end
    else if $l_i = m_i$ *for all* $i = 1, 2, \ldots, r$ **then**
      Done; return $q = m$
    end
    else if $l_i = m_i \pm 1$ ***and*** $l_{i+i} = m_{i+1} \mp 1$ *for all* $i = 1, 2, \ldots, r$*, with wrap-around at* $i = r$*)* **then**
      $s \leftarrow s + 1$ $q_s \leftarrow m$ and $n_s =$ associated number of shifts
    end
  end
  if $s > 0$ **then**
    $ss = \arg\min_s n_s$ (if several minima, pick one with most frequent interior)
    Done; return $q = q_{ss}$
  end
  Find the index j of the shortest run in Q;
  $l_{j-1} \leftarrow l_{j-1} + l_j$;
  $l_i \leftarrow l_{i+1}$ for $i = j, \ldots r - 1$;
  $r \leftarrow r - 1$;
end

For generalized sampling topologies, the database construction and full-field reconstruction are based on *generalized patterns (GPs)*, which have different amounts of overlap with neighboring GPs. We use the following normalization rules for the GPs in order to minimize the entries in the database and to increase the amount of the data for each GP: (i) If the GP is rotationally symmetric, the patterns are rotated so that the longest run is at the top (or left) of the GP; (ii) the level indices start from 0 and consecutively increase if a new level appears in the samples given a pre-specified order of samples; (ii) the levels and level indices have one-to-one correspondence in a GP, including both the sampled and unsampled nodes, independent of other ROIs.

The pattern-based approach is flexible in choosing GPs and sampling topologies. In particular, additional samples can be included from neighboring GPs to propagate global information.

IV. Pattern/MRF Combination

Here we discuss PAT/MRF, the combination of the pattern-based approach with the cutset-MRF approach. As we discussed in the introduction, there is no efficient MRF-based reconstruction for $K > 2$, so the PAT/MRF approach only applies to bilevel cutset reconstruction.

The reconstructions based on both approaches are piecewise smooth in the block interior. However, as we will see in Section VI, the performance of the cutset-MRF approach is heavily

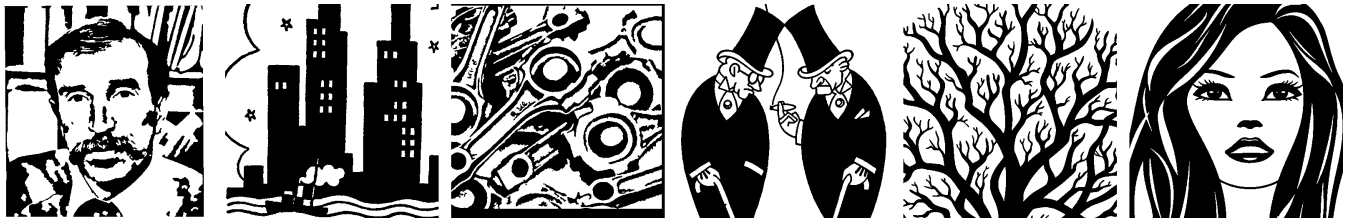

Fig. 6: Examples of complex bilevel images

Fig. 7: Examples of simple bilevel images

dependent on the connection bits. On the other hand, the pattern-based approach bases the structural decisions (whether two runs should be connected) on natural image statistics, without the need for connection bits. Otherwise, i.e., when the same runs are connected, the segment contours generated by the two approaches are similar, although the pattern-based approach tends to preserve finer details. The two approaches can be combined in such a way that the connection choices are based on the statistics of the pattern-based approach, while the patterns are approximated by the MRF model given the connections. Specifically, the cutset block pattern database is constructed as described in Section III. We then consider one, two, or more reconstructions based on the MRF approach depending on the number of runs and associated connection bits (up to 4). We compare these MRF reconstructions with the pattern-based reconstruction and select the one that minimizes the error rate. The selection can be represented as one or a few connection bits [2], [3], which requires considerably less storage than the $(N-1)^2$ pixels for each block pattern in the database. As in [3], we base all MRF-based reconstructions on digital straight lines using Bresenham's approximation [21].

When enough connection bits are used, the structural choices are the same, and the only difference in the two reconstructions is that curved lines are replaced with straight lines, that is, the pattern-based approach preserves finer details. This combination largely reduces the memory for storing the reconstruction codebooks, and thus, also the testing time.

V. Cutset Sampling and Segmentation

In this section we consider cutset sampling of a grayscale or color image and segmenting the cutset. The reconstruction of the full segmentation field can then be done as described in the previous sections.

Figure 8 shows an original image in (a) and the cutset samples in (b). The segmentation is done using the adaptive clustering algorithm (ACA) [8]. Applying to the pixels on the cutset requires minor adjustments to account for the fact that the image samples and segment labels exist only on the cutset. In fact, all we need to do is use a fixed label for the pixels that are not on the cutset, and proceed with the segmentation as in the full grid case. The conditional probabilities and local intensity functions are estimated using only the pixels on the grid. The results are shown in Figure 8(c) and compared with the full ACA segmentation in (d) and the corresponding cutset in (e). Note that the resulting segments in the cutsets are comparable. More results will be presented in Section VI-G.

VI. Experimental Results

A. Experiment Setup

In our experiments we used three datasets: (i) an in-house bilevel dataset including 13 fairly complex bilevel images; examples are shown in Figure 6; (ii) a large collection of relatively simple bilevel images of single objects (5578 images) [22]; examples are shown in Figure 7; and (iii) BSDS500, a dataset of K-level images obtained by human segmentations of 500 natural images [23]; examples are shown in Figure 4.[1]

The BSDS500 dataset is partitioned into a training set (200 original images, 1087 segmentations), a test set (200 original images, 1063 segmentations), and a validation set (100 original images, 546 segmentations) [23]. We used the training set to construct the pattern database segmentations and the test set for algorithm evaluation. The training and test sets were completely separate. We did not make use of the validation set, as there were no parameters to be estimated.

The training partition contains adequate numbers of both bilevel and K-level patterns for database construction. The cutsets were sampled and reconstructed at multiple cutset sampling steps, N. We will use PAT to refer to the pattern-based approach, and PM to refer to the PAT/MRF combination. These approaches were implemented in C++. The cutset-MRF approaches, based on the second-order MRF model (MRF_2) and the hybrid MRF approach (MRF_h), were tested on the bilevel images and compared with the pattern-based approaches.

In addition, we implemented two baseline interpolation methods adapted for images that consist of region labels without any quantitative significance. The first is a *nearest neighbor (NN)* approach, whereby an interior pixel takes the value of the closest boundary point. The second is a *variation* of *bilinear interpolation (BL)*, whereby we find the closest point in each of the four linear segments of the block boundary (top, bottom, left, and right), and weigh its label by the fraction of its distance from the opposite side, as in bilinear interpolation. However, since it does not make sense to compute a weighted sum of pixel labels, we only combine weights for equal labels and then simply pick the label with the highest weight.

B. Block Statistics

Table I lists the percentage of nonuniform blocks in the training partition of the BSDS500 dataset with different combinations of

[1]These datasets can be found at drive.google.com/file/d/1HqUsJ359l-M2At1UOZIYKpd-HQQhzX8H

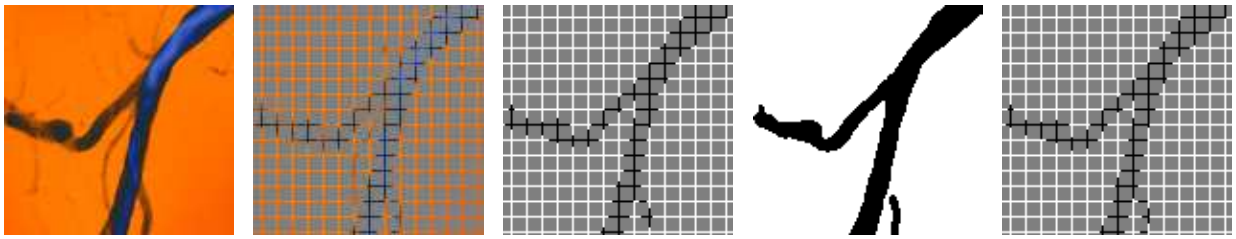

Original Cutset Samples Cutset Segmentation ACA Segmentation Cutset of ACA Segm.

Fig. 8: Cutset sampling and segmentation versus segmentation and cutset sampling of the original image

TABLE I: BSDS500 Block Statistics: Percentage of blocks with K levels and R runs for cutset sampling steps N

	$N=8$							$N=16$						
$K\backslash R$	2	3	4	5	6	7	8	2	3	4	5	6	7	8
2	85	0	4.6	0	0.3	0	.03	73	0	6.8	0	0.9	0	0.2
3	0	3.6	4.5	0.2	0.3	.01	.03	0	5.2	8.1	0.6	1.1	0.1	0.2
4	0	0	0.3	0.3	0.2	.02	.03	0	0	0.8	0.9	0.9	0.1	0.2
5	0	0	0	.02	.04	.02	.01	0	0	0	0.1	0.2	0.1	0.1

numbers of levels K and runs R for cutset sampling steps 8 and 16. The number of nonuniform blocks, i.e., blocks with at least two levels, in this database is of the order of 10^7, resulting from 10^3 human segmentations of 200 training images. Bilevel blocks are the most common and can only have an even number of runs, i.e., black and white runs appear in pairs. Three-level blocks are also quite common. In the training data, the number of levels and runs in a block are bounded by $K \leq 8$, $R \leq 14$ when $N = 8$, and $K \leq 24$, $R \leq 11$ when $N = 16$, respectively. When $N = 8$, the blocks with $K > 4$ or $R > 6$ only account for less than 0.1% of the total. When $N = 16$, the blocks with $K > 5$ or $R > 8$ only account for less than 0.1% of the total. Therefore, considering the connections of up to 4 pairs of black and white runs in bilevel images are enough to cover 99.9% of the nonuniform blocks. In K-level image reconstruction, processing blocks independently reduces the number of levels to consider, thus reducing complexity. The statistics are similar for blocks obtained with other cutset sampling steps.

C. Block Reconstructions

Figure 9 shows examples of normalized 2-level cutset block boundaries, normalized original blocks collected in the training set, and local reconstructions from the boundaries based on PAT, MRF_2, and MRF_h, as well as the NN and BL interpolations. PAT determines the most probable (on a pixel-by-pixel basis) reconstruction pattern for a given a boundary specification. In some cases, the PAT reconstructions are similar to those of MRF_2 or MRF_h but, overall, PAT is much better at preserving image structure. The NN and BL reconstructions are clearly worse than those of the other approaches.

The PM reconstructions (not shown in the figure) have the same structure as the PAT reconstructions, with curved lines replaced with straight lines. Note that we refer to digital straight lines using Bresenham's approximation [21] as *straight* lines, and all other lines as *curved*. While straight line contours are often favored by PAT, curvy contours are also possible, as the examples in the second and last rows of Figure 9 and the third row of Figure 10 demonstrate.

The last row of Figure 9 shows a case where the black and white runs are almost symmetric. In this case, PAT reconstructs the most likely pattern with curvy contours, MRF_2 prefers the reconstruction with shorter segment contours, while MRF_h considers the two reconstructions (shown in the last two columns) equally likely and picks one randomly or based on a preset preference.

Figure 10 shows examples of normalized 3-level cutset block boundaries, normalized original blocks collected in the training set, and local reconstructions from the boundaries based on PAT and the NN an BL interpolations. The NN approach reconstructions are clearly inferior but the BL reconstructions look reasonable. However, as we will see below, their overall performance on the entire image is significantly worse than that of the pattern-based approach.

D. Visual Results

Figure 11 shows the K-level reconstruction results of the PAT approach for $N = 8$ and the challenging sampling step $N = 16$. Note that the PAT approach preserves most of the segment structure for $N = 8$ and misses some of the finer details for $N = 16$. The figure also shows the NN and BL reconstructions for $N = 8$, which are clearly worse than those of the PAT approach. The $N = 16$ reconstructions (not shown) are equally poor.

Figure 12 shows reconstruction results for bilevel cutsets with the typical sampling step of 8. The figure shows that the proposed approaches, PAT and PM, clearly outperform the NN and BL interpolations and MRF_2 without connection bits, and come very close to MRF_2 with connection bits. The performance of MRF_h is also significantly better than MRF_2, but inferior to PAT as can be seen in the broken lines of images in the second and third row of Figure 12. PAT also reduces the number of isolated one-pixel-wide runs in the reconstruction compared to the MRF approaches. As we discussed, PMselects the most probable connections based on the statistics collected by PAT and reconstructs piecewise smooth contours.

The pattern-based approach can also be applied to general sampling topologies with periodic structures. The first row of Figure 13 shows examples of various sampling topologies and the other rows show the reconstructions from such sampling topologies. Note that the sampling densities are similar but not directly comparable. Systematic comparisons will presented in the next subsection. The figures show that when the cutset GPs consist of connected samples, that is, the block interiors can be reconstructed from the boundaries independently of the other blocks, as in the rectangular and hexagonal topologies, the reconstructions are smoother and better preserve the image

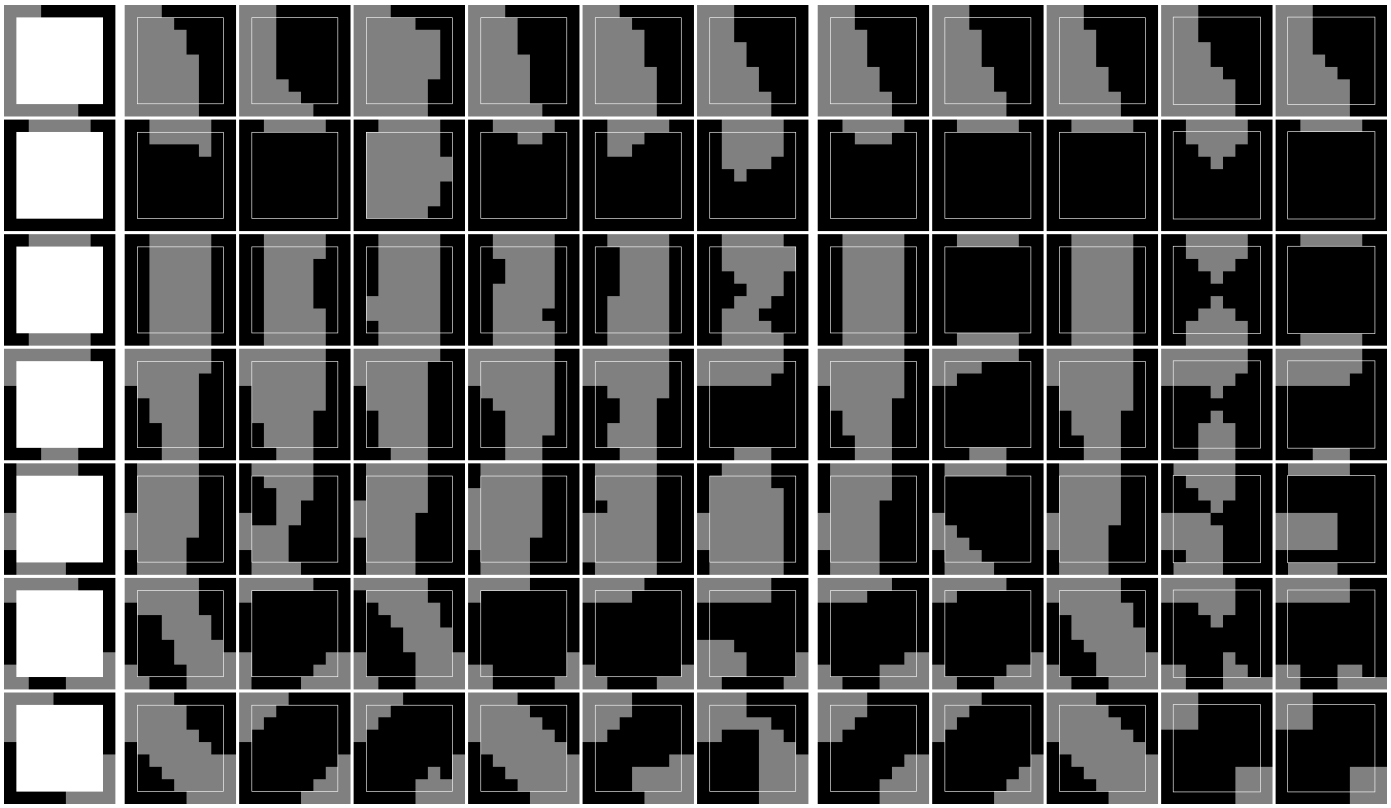

Fig. 9: Boundary specifications ($K = 2$); examples (1-6) of normalized patterns with the same or similar boundaries; retrieved block patterns (PAT); reconstructions by cutset-MRF model (MRF_2); hybrid MRF model (MRF_h); NN and BL interpolation.

structure than those obtained with polyline (e.g., zig-zag) or random topologies, where the GPs are not connected.

E. Reconstruction Error Rate

Table II shows the reconstruction error rate with cutset sampling steps $N = \{16, 14, \ldots, 2\}$ based on various reconstruction approaches in the three datasets. The associated variances are shown in Table III for $N = 16$ and $N = 8$. Note that for square cutsets, the number of cutset samples is smaller than that of the unsampled nodes to be reconstructed when $N \geq 6$. PAT outperforms the MRF approaches in both bilevel and K-level reconstructions. Note that, as expected, the reconstruction error rate for PM lies between that of MRF_h and PAT. The lower PM error rate compared to MRF_h is mainly due to the higher percentage of blocks with correct connectivities of runs. PM has higher error rate than PAT because it uses straight lines to approximate PAT. Finally, the performance of the NN and the modified BL approaches is clearly inferior to the pattern-based and MRF-based approaches.

To determine the significance of the differences in the reconstruction error rates, we conducted a Kruskal-Wallis H test [24], which is a non-parametric method for testing whether two sets of samples originate from the same distribution. Since the in-house bilevel image dataset includes only 13 images, we combined it with the bilevel shape dataset for the test. The results are shown in Table IV, and demonstrate the significance of the performance differences. More importantly, as Figures 12 and 11 demonstrate, the differences are *perceptually* significant.

We also compare the reconstruction error rate for the different sampling topologies. Since the number of samples on the cutset is not the same for the different topologies, we plotted the reconstruction error rate versus the normalized wire length needed to connect the sensors. This assumes that the sensor cost is negligible and that the only cost is the length of wire needed to connect the sensors. We chose wire length for simplicity. Alternative wireless communications schemes among the sensors can also be considered, as in [4].

The wire needed to connect the sensors in each geometry is illustrated in Fig. 14. Note that, since the data in our simulations is given on a Cartesian grid, for hexagonal sampling, the samples are not on perfect hexagons; the green lines show the hexagons that that the border samples approximate. The hexagonal sampling is specified by three parameters (h, w, l), the height and width of the cutset block and the length of the vertical edge of the block, respectively. The wire length for each geometry can be calculated as follows. Assume that we are sampling an $m \times n$ Cartesian grid. For a $u \times u$ uniform topology, we need wire to connect m/u rows of length $n - 1$ and one column of length $m - 1$. The total wire length is

$$l_{\text{unif}} = \frac{m(n-1)}{u} + m - 1 \tag{5}$$

For a $r \times r$ rectangular topology, we need wire to connect m/r rows of length $n-1$ and n/r columns of length $m-1$. The total wire length is

$$l_{\text{rect}} = \frac{m(n-1)}{r} + \frac{n(m-1)}{r} \tag{6}$$

For a line topology with l horizontal spacing, we need wire to connect n/l columns of length $m - 1$ and one row of length 1.

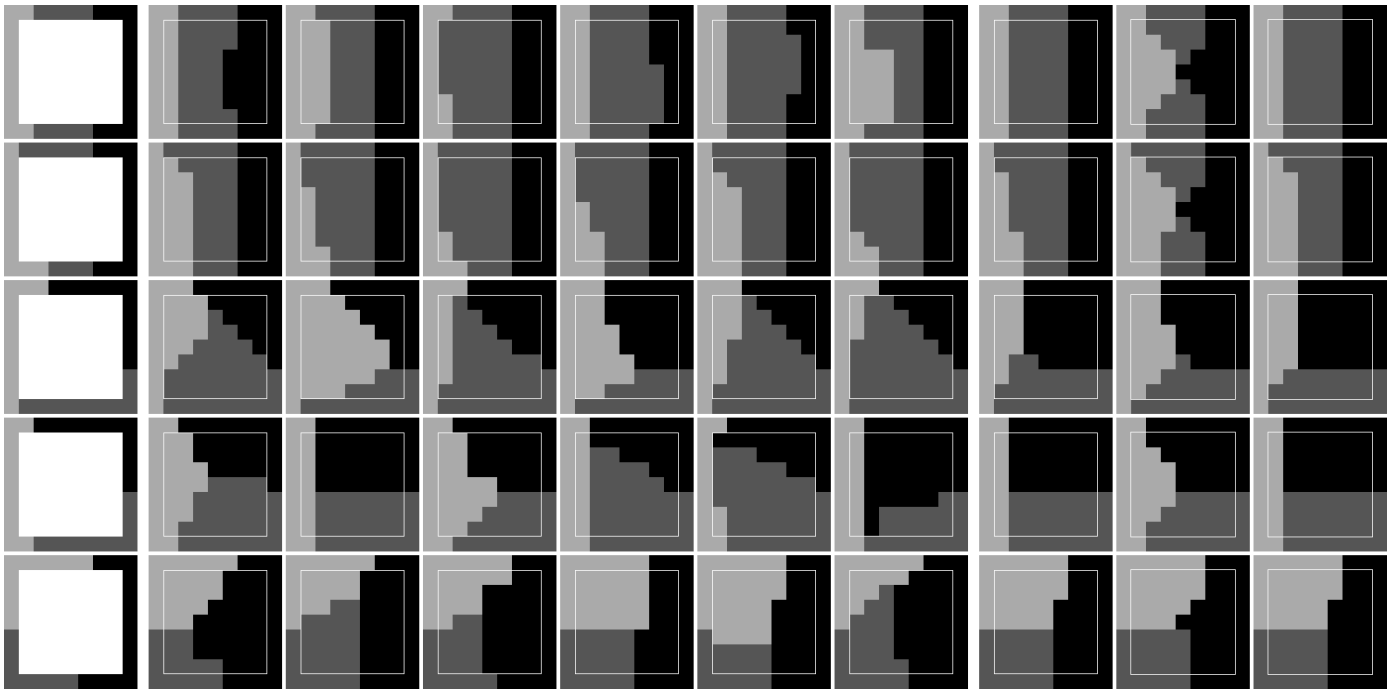

Fig. 10: Boundary specifications ($K = 3$); examples (1-6) of normalized patterns with the same or similar boundaries; retrieved block patterns (PAT); NN and BL reconstructions.

TABLE II: Average reconstruction error rate

	In-house bilevel image dataset								Bilevel shape dataset [22]								K-level dataset				
N	[15]	[17]	MRF_2	MRF_h	PAT	PM	NN	BL	[15]	[17]	MRF_2	MRF_h	PAT	PM	NN	BL	[15]	[17]	PAT	NN	BL
16	.075	.069	.071	.049	**.047**	.048	.066	.067	.064	.054	.047	.043	**.039**	.042	.050	.043	.035	.068	**.016**	.031	.024
14	.065	.061	.061	.042	**.039**	**.039**	.061	.062	.056	.047	.040	.036	**.033**	.035	.046	.038	.031	.058	**.014**	.027	.020
12	.056	.053	.050	.034	**.031**	.032	.053	.053	.048	.042	.033	.029	**.026**	.028	.041	.033	.026	.046	**.011**	.024	.017
10	.047	.044	.038	.027	**.024**	.025	.045	.042	.040	.035	.025	.023	**.020**	.022	.037	.026	.021	.036	**.009**	.020	.014
8	.038	.035	.027	.019	**.017**	.018	.035	.031	.032	.029	.018	.017	**.015**	.016	.031	.020	.017	.025	**.007**	.016	.011
6	.027	.025	.016	.013	**.011**	.012	.027	.021	.022	.020	.013	.012	**.011**	**.011**	.022	.014	.012	.016	**.005**	.012	.008
4	.015	.015	**.007**	**.007**	**.007**	**.007**	.018	.011	.012	.012	**.006**	**.006**	**.006**	**.006**	.015	.008	.007	.007	**.003**	.008	.005
2	.005	.003	**.002**	**.002**	**.002**	**.002**	.007	.004	.003	**.002**	**.002**	**.002**	**.002**	**.002**	.006	**.002**	.002	**.001**	**.001**	.003	.002

TABLE III: Standard deviation of reconstruction error rate

	In-house bilevel image dataset						Bilevel shape dataset [22]						K-level dataset		
N	MRF_2	MRF_h	PAT	PM	NN	BL	MRF_2	MRF_h	PAT	PM	NN	BL	PAT	NN	BL
16	.040	.028	**.030**	.027	.030	.039	.022	.017	**.015**	.017	.014	.015	**.010**	.014	.011
8	.015	.011	**.010**	.010	.016	.018	.010	.008	**.007**	.007	.008	.007	**.004**	.007	.006

The total wire length is

$$l_{\text{line}} = \frac{n(m-1)}{l} + n - 1 \tag{7}$$

For a $z \times z$ zig-zag topology with diagonal lines, we need wire to connect n/z columns of length $\sqrt{2}(m-1)$ and one row of length $n-1$. The total wire length is

$$l_{\text{zigz}} = \frac{\sqrt{2}\, n(m-1)}{z} + n - 1 \tag{8}$$

For a (h, w, l) hexagonal topology, the pattern is periodic with period $(h+l) \times w$, so there are a total of $\frac{n}{h+l}\frac{m}{w}$ periods. However, the wire length of each period depends on the particular parameters. For $(4, 4, 2)$ and $(8, 8, 4)$, each period has length $2(h+w)$ for a total wire length of

$$l_{\text{hexa}} = \frac{n}{h+l}\,\frac{m}{w}\,2(h+w) \tag{9}$$

For $(19, 16, 9)$, each period has length $2l + 4(5 + 4 \cdot \sqrt{2})$ for a total wire length of

$$l_{\text{hexa}} = \frac{n}{h+l}\frac{m}{w}(2l + 4(5 + 4 \cdot \sqrt{2})) \tag{10}$$

Since the dominant term is each of the above length formulas is mn, it is natural to use it as the normalization factor.

Since the image size is not always an exact multiple of the cutset block, we extend the images to the right and bottom by repeating pixels until complete cutset blocks are formed, and after reconstruction, we remove the pixels beyond the original image boundary. An example can be found in the supplemental material. For hexagonal sampling, this has to be done on all four sides of the image.

Figure 15 plots the reconstruction error rate versus the normalized wire length averaged over each of the three datasets. In our wire length calculations, we took into account the extra wire

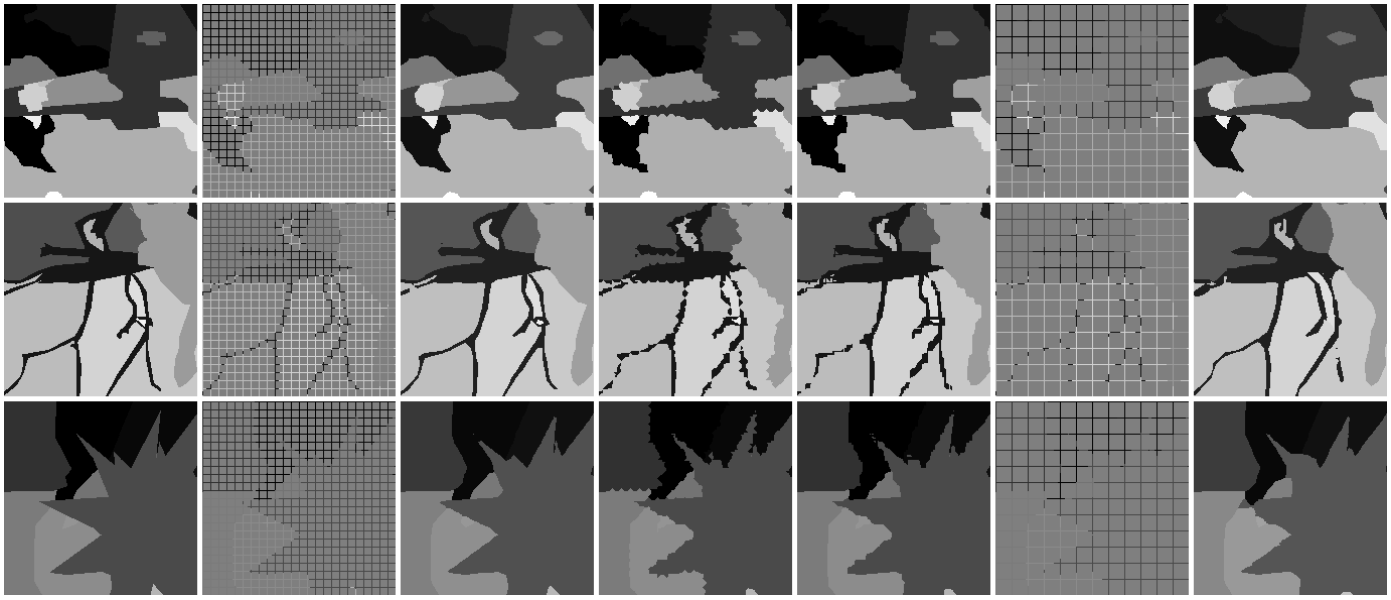

Fig. 11: Reconstructions of K-level images from cutsets with sampling steps 8 and 16. Images cropped for display.

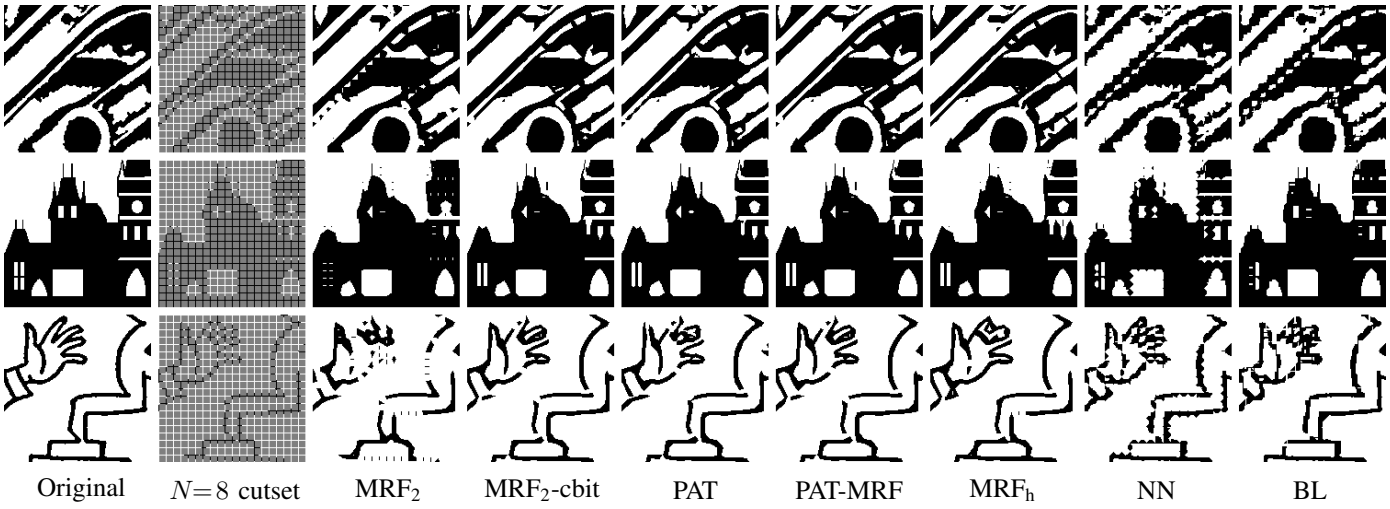

Fig. 12: Reconstruction of bilevel images from cutsets with sampling step 8. Images cropped for display.

TABLE IV: Kruskal-Wallis H Test

	Combined bilevel in-house image and shape [22] datasets					K-level dataset	
N	PAT vs. MRF_2	PAT vs. MRF_h	PAT vs. PM	PAT vs. NN	PAT vs. BL	PAT vs. NN	PAT vs. BL
16	1.35 E-123	3.89 E-44	1.83 E-26	0.00 E+00	2.72 E-47	1.06 E-155	8.40 E-59
8	1.11 E-68	1.78 E-31	2.67 E-06	0.00 E+00	0.00 E+00	6.72 E-223	1.73 E-100

needed to complete the cutsets on the boundaries, even though this is not reflected in (5) – (10). Details can be found in the supplemental materials. For each of the cutset topologies, we consider three sampling steps, $(4, 4, 2)$, $(8, 8, 4)$, and $(19, 16, 9)$ for the hexagonal, and 4, 8, and 16 for the other topologies.

Observe that uniform sampling is clearly suboptimal in the error-wirelength plots. The performance of the other topologies is comparable, providing different operating points along a curve. However, we could argue that the rectangular topology performs best on average followed by the zig-zag and lines topologies, while the $(4, 4, 2)$ hexagonal is clearly inferior on the bilevel shape dataset.

F. Computational Cost

The algorithms were implemented in C++ and ran on a laptop with a 2.2 GHz Intel Core i7 processor and 16 GB 1600 MHz DDR3 memory. Table V lists the average time for reconstructing a 512 $\times$ 512 image. The codebook is loaded into the memory once prior to reconstruction, which is the main factor for consumption of computational resources. Consequently, the codebook size directly impacts test time. When combined with MRFs, the codebook size in the database for PM is reduced, which consequently reduces the test time. The processing of bilevel images requires less time than that of the K-level images. The block sizes make a difference in pattern-based approaches mainly due to the resulting size of codebooks.

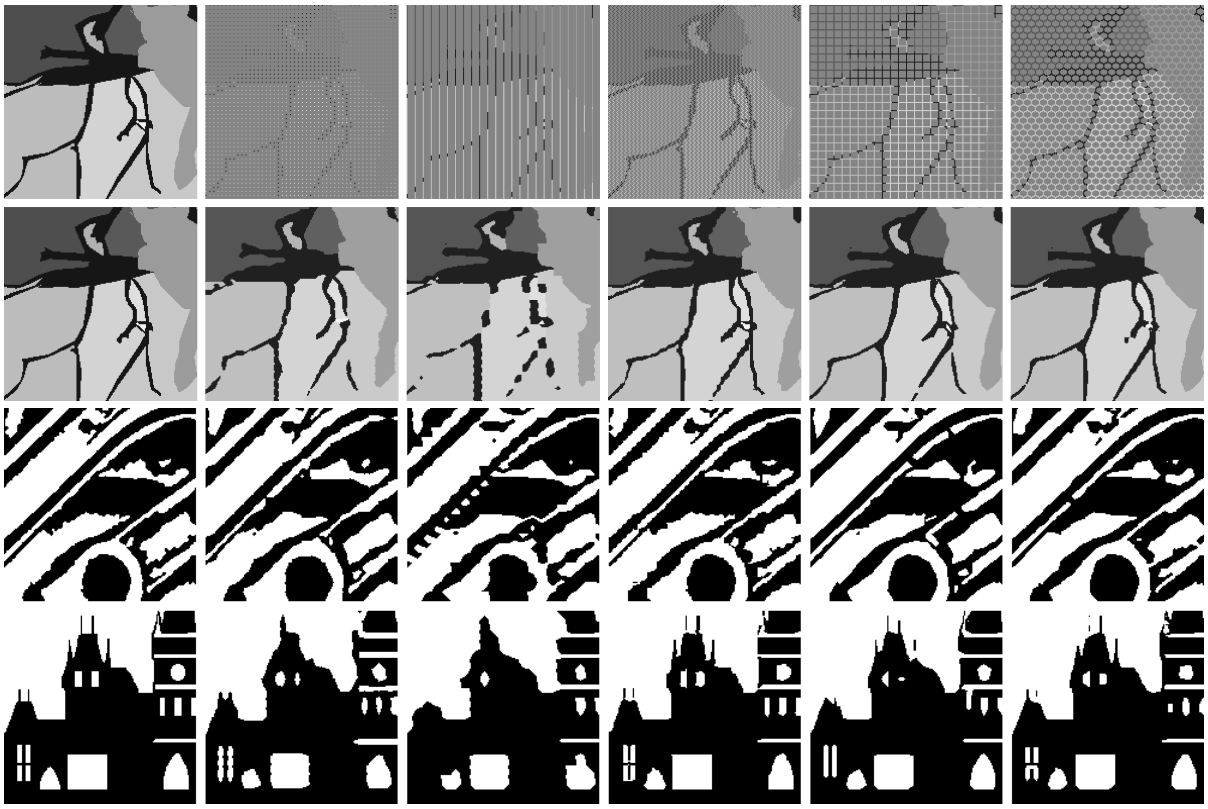

Fig. 13: Sampling (first row) and reconstruction for generalized cutsets

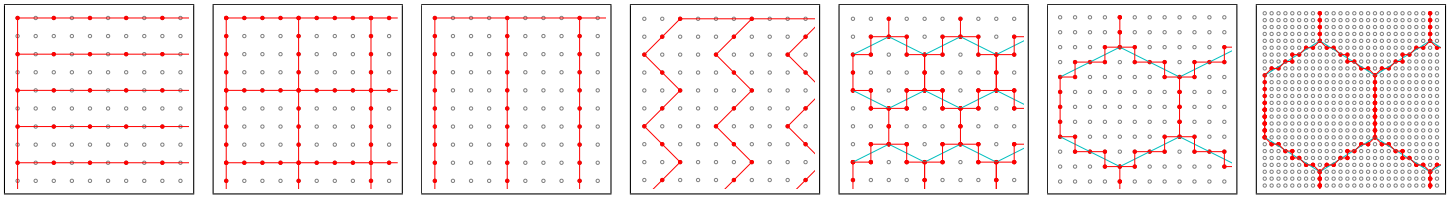

Fig. 14: Sensor wire connections for different cutset geometries

TABLE V: Average time (sec) for reconstructing 512×512 image

Methods	Bilevel				K-level
	MRF_2	MRF_h	PAT	PM	PAT
N = 16	0.007	0.007	1.253	0.008	1.480
N = 8	0.005	0.005	0.082	0.007	0.119

G. Cutset Sampling, Segmentation, and Reconstruction

Figure 16 shows an original color image, the cutset samples, the segmentation of the cutset samples, and the reconstruction from the cutset segments, and compares the latter to the segmentation of the full image. Note that the resulting segments are comparable. In fact, the full image segmentation detects some spurious segments in the upper right edge, which are not present in the cutset segmentation and reconstruction. Figure 17 shows another example, where the main structures (a "river" and a "lake") are preserved by both approaches. Note that, in this figure, the segments have been "painted" with their average color.

VII. Conclusions

We introduced a pattern-based approach for K-level cutset reconstruction that utilizes the statistics of human segmentations to generate a codebook of patterns for reconstruction. The pattern-based approach also applies to a broader class of images, including K-level images ($K \geq 2$), and general sampling topologies, such as non-intersecting lines, hexagonal cutsets, and uniform point samples. The pattern-based approach and the MRF model were then combined for bilevel cutset reconstruction, utilizing human segmentation statistics to determine structural information, while generating the reconstruction details based on the MRF model. This reduces the codebook size, and consequently the computation time, with the reconstruction error rate between that of pattern-based approach and hybrid cutset-MRF approach. In addition, we presented an algorithm for segmenting the cutset samples of an original grayscale or color image, followed by reconstruction of the full segmentation field via the pattern-based approach. Experimental results demonstrate that the proposed approaches outperform the cutset-MRF approaches in terms of both reconstruction error rate and perceptual quality. A systematic

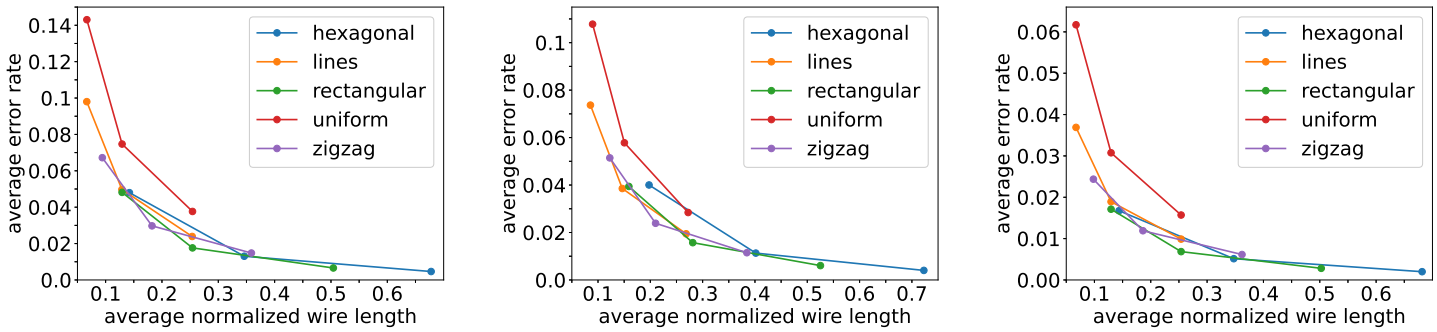

(a) In-house bilevel dataset (b) Bilevel shape dataset (c) K-level dataset

Fig. 15: Reconstruction error rate versus normalized wire length for different cutset geometries

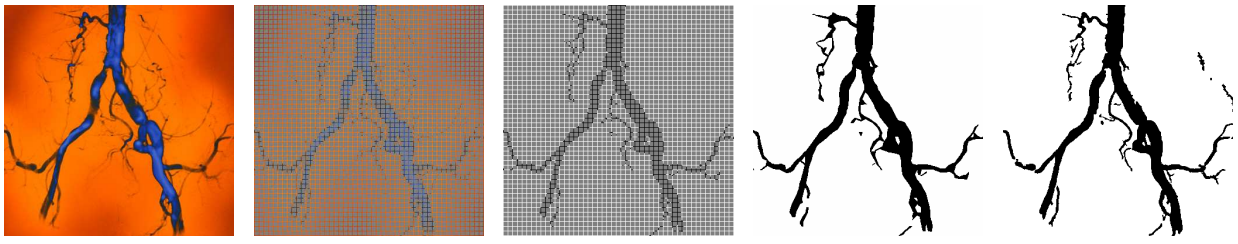

Original Cutset Samples Cutset Segmentation Cutset Reconstruction ACA Segmentation

Fig. 16: Cutset sampling, segmentation, and reconstruction

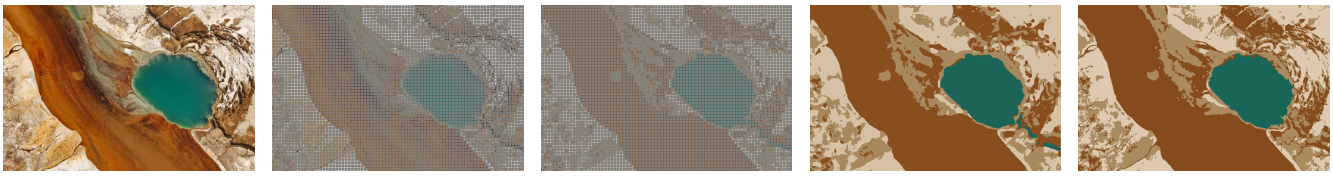

Original Cutset Samples Cutset Segmentation Cutset Reconstruction ACA Segmentation

Fig. 17: Cutset sampling, segmentation, and reconstruction

comparison of the reconstruction error rate versus the normalized wire length needed to connect the sensors shows that the performance of the different cutset topologies is comparable and significantly better than uniform sampling. Finally, we believe that introducing global information can further improve the cutset reconstruction quality.

REFERENCES

[1] M. G. Reyes, X. Zhao, D. L. Neuhoff, and T. N. Pappas, "Lossy compression of bilevel images based on Markov random fields," in *Proc. Int. Conf. Image Proc. (ICIP)*, vol. 2, San Antonio, TX, Sep. 2007, pp. II–373–II–376.

[2] M. G. Reyes, D. L. Neuhoff, and T. N. Pappas, "Lossy cutset coding of bilevel images based on Markov random fields," *IEEE Trans. Image Process.*, vol. 23, no. 4, pp. 1652–1665, Apr. 2014.

[3] S. Zha, T. N. Pappas, and D. L. Neuhoff, "Hierarchical lossy bilevel image compression based on cutset sampling," *IEEE Trans. Image Process.*, vol. 30, pp. 1527–1541, 2021.

[4] M. A. Prelee and D. L. Neuhoff, "Performance-energy tradeoffs in cutset wireless sensor networks," in *Proc. Int. Conf. Acoustics, Speech, Signal Proc. (ICASSP)*, Florence, Italy, May 2014, pp. 7585–7589.

[5] A. Farmer, A. Josan, M. A. Prelee, D. L. Neuhoff, and T. N. Pappas, "Cutset sampling and reconstruction of images," in *Proc. Int. Conf. Image Proc. (ICIP)*, Brussels, Belgium, Sep. 2011, pp. 1909–1912.

[6] M. A. Prelee, D. L. Neuhoff, and T. N. Pappas, "Image reconstruction from a Manhattan grid via piecewise plane fitting and Gaussian Markov random fields," in *Proc. Int. Conf. Image Proc. (ICIP)*, Orlando, FL, Oct. 2012, pp. 2061–2064.

[7] M. A. Prelee, D. L. Neuhoff *et al.*, "Image interpolation from manhattan cutset samples via orthogonal gradient method," in *Proc. Int. Conf. Image Proc. (ICIP)*, 2014, pp. 1842–1846.

[8] T. N. Pappas, "An adaptive clustering algorithm for image segmentation," *IEEE Trans. Signal Process.*, vol. SP-40, no. 4, pp. 901–914, Apr. 1992.

[9] S. Zha and T. N. Pappas, "Pattern-based K-level cutset reconstruction," in *Proc. Int. Conf. Image Processing (ICIP)*. Quebec City, Canada: IEEE, Sep. 2015, pp. 3344–3348.

[10] ——, "Generalized K-level cutset sampling and reconstruction," in *Proc. Int. Conf. Acoustics, Speech, and Signal Processing (ICASSP)*. Shanghai, China: IEEE, Mar. 2016, pp. 1681–1685.

[11] S. Zha, T. N. Pappas, and D. L. Neuhoff, "Hierarchical bilevel image compression based on cutset sampling," in *Proc. Int. Conf. Image Processing (ICIP)*, Orlando, FL, Oct. 2012, pp. 2517–2520.

[12] M. A. Prelee and D. L. Neuhoff, "Multidimensional manhattan sampling and reconstruction," *IEEE Trans. Inf. Theory*, vol. 62, no. 5, pp. 2772–2787, 2016.

[13] S. Zha and T. N. Pappas, "A hybrid Markov random field model for bilevel cutset reconstruction," in *Proc. Int. Conf. Image Processing (ICIP)*. Phoenix, AZ: IEEE, Sep. 2016, pp. 3523–3527.

[14] M. A. Prelee and D. L. Neuhoff, "Energy efficient source localization on a manhattan grid wireless sensor network," in *Proc. Int. Conf. Acoustics, Speech, Signal Proc. (ICASSP)*, 2013, pp. 4266–4270.

[15] M. Bertalmio, A. L. Bertozzi, and G. Sapiro, "Navier-stokes, fluid dynamics, and image and video inpainting," in *IEEE Conf. Computer Vision and Pattern Recognition (CVPR)*, vol. I, Kauai, HI, Dec. 2001, pp. I–355–I–362.

[16] A. L. Bertozzi, S. Esedoglu, and A. Gillette, "Inpainting of binary images using the cahn-hilliard equation," *IEEE Trans. Image Process.*, vol. 16, no. 1, pp. 285–291, 2007.

[17] A. Telea, "An image inpainting technique based on the fast marching method," *Journal of graphics tools*, vol. 9, no. 1, pp. 23–34, 2004.

[18] A. Criminisi, P. Pérez, and K. Toyama, "Region filling and object removal by exemplar-based image inpainting," *IEEE Trans. Image Process.*, vol. 13, no. 9, pp. 1200–1212, 2004.
[19] J.-B. Huang, S. B. Kang, N. Ahuja, and J. Kopf, "Image completion using planar structure guidance," *ACM Trans. Graphics (Proc. SIGGRAPH 2014)*, vol. 33, no. 4, p. 129, 2014.
[20] S. M. A. Eslami, N. H. C. K. I. Williams, and J. Winn, "The shape Boltzmann machine: A strong model of object shape," *Int. J. Comput. Vis.*, vol. 107, pp. 155–176, 2014.
[21] J. E. Bresenham, "Algorithm for computer control of a digital plotter," *IBM Systems Journal*, vol. 4, no. 1, pp. 25–30, Mar. 1965.
[22] B. Kimia, "A large binary image database," http://www.lems.brown.edu/~dmc/, 2002, accessed: 2015-01-10.
[23] P. Arbelaez, M. Maire, C. Fowlkes, and J. Malik, "Contour detection and hierarchical image segmentation," *IEEE Trans. Pattern Anal. Mach. Intell.*, vol. 33, no. 5, pp. 898–916, May 2011.
[24] W. H. Kruskal and W. A. Wallis, "Use of ranks in one-criterion variance analysis," *J. Amer. Statistical Assoc.*, vol. 47, no. 260, pp. 583–621, 1952.

Shengxin Zha received the B.S. degree in electrical engineering from the Xi'an Jiaotong University in 2010, and the M.S. and Ph.D. degrees from Northwestern University in electrical and computer engineering and electrical engineering, respectively. In 2016 she joined Facebook as a research engineer, and since 2020, as a technical lead manager. Here research interests are in image processing, computer vision, AI, and machine learning.

Daizong Tian received the B.S. degree in telecommunications engineering with management from Beijing University of Posts and Telecommunications, Beijing, China, in 2019, and the M.S. degree from Northwestern University in electrical engineering, in 2021, where he is currently pursuing a Ph.D. degree. His research interests are in image processing, computer vision, computational imaging, and machine learning.

Thrasyvoulos N. Pappas (M'87, SM'95, F'06) received the S.B., S.M., and Ph.D. degrees in electrical engineering and computer science from MIT in 1979, 1982, and 1987, respectively. From 1987 until 1999, he was a Member of the Technical Staff at Bell Laboratories, Murray Hill, NJ. In 1999, he joined the ECE Department at Northwestern University. His research interests are in human perception and electronic media, and in particular, image quality and compression, image analysis, content-based retrieval, model-based halftoning, and tactile and multimodal interfaces. Prof. Pappas is a Fellow of SPIE and IS&T. He has served as Editor-in-Chief of the IEEE Transactions on Image Processing, Vice President-Publications for the Signal Processing Society (SPS) of IEEE, and co-chair of SPIE/IS&T Human Vision and Electronic Imaging Conference. He is currently Editor-in-Chief of the IS&T Journal of Perceptual Imaging.